Leading edge erosion detection for a wind turbine blade using far-field aerodynamic noise

Zhang, Yanan; Avallone, Francesco; Watson, Simon

DOI
10.1016/j.apacoust.2023.109365

Publication date
2023

Document Version
Final published version

Published in
Applied Acoustics

Citation (APA)
Zhang, Y., Avallone, F., & Watson, S. (2023). Leading edge erosion detection for a wind turbine blade using far-field aerodynamic noise. *Applied Acoustics*, *207*(2023), Article 109365. https://doi.org/10.1016/j.apacoust.2023.109365

Applied Acoustics 207 (2023) 109365

Contents lists available at ScienceDirect

Applied Acoustics

journal homepage: www.elsevier.com/locate/apacoust

Leading edge erosion detection for a wind turbine blade using far-field aerodynamic noise

Yanan Zhang [a,*], Francesco Avallone [b], Simon Watson [a]

[a] Wind Energy Section, Faculty of Aerospace Engineering, Delft University of Technology, Delft 2629HS, The Netherlands
[b] Department of Mechanical and Aerospace Engineering, Politecnico di Torino, Turin 10129, Italy

ARTICLE INFO

Article history:
Received 22 June 2022
Received in revised form 26 January 2023
Accepted 29 March 2023

Keywords:
Wind turbine blade
Leading edge erosion
Aerodynamic noise
Damage detection
Aeroacoustics

ABSTRACT

In this paper, the feasibility of using far-field acoustic measurements as a non-contact monitoring technique for wind turbine blade leading edge erosion is assessed. For this purpose, a DU96 W180 airfoil with several eroded leading edge configurations of different severities is experimentally investigated. The eroded leading edges are designed with pits, gouges and coating delamination scaled from a real eroded blade. To assess the feasibility of the technique in quasi-realistic configurations, experiments are carried out under clean and turbulent inflow conditions. Acoustic measurements are performed with a phased microphone array. In the absence of inflow turbulence, because of the low Reynolds number at which the experiments are carried out, the case with minor erosion severity shows similar far-field noise spectra as the clean leading-edge cases, i.e., the presence of tonal peaks caused by laminar boundary layer instability noise through a self-sustained feedback loop but with higher tonal amplitudes. Increasing the damage level (considered as moderate erosion), the spectra of the noise scattered from the suction side show that the tonal peaks shift to higher frequencies and have lower amplitudes, thus suggesting that the damage alters the flow features responsible for the acoustic feedback loop; whereas, the spectra from the pressure side show a broadband noise distribution. For heavy erosion, the far-field noise spectra show broadband features from both airfoil sides, thus suggesting that the damage has fully forced the transition to turbulent flow; in which case, an increase in the low-frequency content is observed. Conversely, in the presence of turbulent inflow, when comparing the noise scattered at the trailing edge, no difference is found. However, leading edge impingement noise decreases at medium–high frequency compared with the baseline case at a chord-length-based Strouhal number $St_C \sim 10$. The experimental results also suggest that the delamination feature is the one which is the most easily detectable and the approach is valid for a wide range of angles of attack and inflow velocity.

1. Introduction

Leading edge erosion is one of the most observed damage types on wind turbine blades. During the operational life of a wind turbine, aside from the aging of the blades, raindrops or hail, and other solid particles, such as sand grains, are the principal external contributors to blade leading edge erosion [1–3]. At the very first stage, damage often appears as small, randomly distributed pits; then as the damage develops, larger-size gouges occur; these pits and gouges grow in size and density leading to coating delamination on the surface [4]. This results in a reduction in the lift of the blade, therefore a loss of power output [5–7].

Power conversion efficiency or turbine efficiency is often considered as a priority in the wind power industry. Therefore, most of the research on leading edge erosion has concentrated mainly on how the erosion affects the aerodynamic performance of the blades [4,8–10]. However, it is essential to detect erosion and monitor the development of damage, not only to provide a reliable prediction of power output but more importantly to reduce potential operational risks for a wind farm. Therefore, the development of a reliable, flexible and low-cost damage detection technique is of high relevance to the wind power industry [11].

A few studies [1,3,12] have focused on the mechanism of erosion formation and growth aiming at building dynamic models to predict the potential lifetime of a blade and any consequential effect on the annual energy production. These models account for blade material properties, operational (e.g. wind and rotor speed) and environmental (sizes of raindrops or sands) conditions. They

---

* Corresponding author.
E-mail address: Yanan.Zhang@tudelft.nl (Y. Zhang).

https://doi.org/10.1016/j.apacoust.2023.109365
0003-682X/© 2023 The Authors. Published by Elsevier Ltd.

provide good predictions for blade lifetime and the timing for inspections but cannot be used for real-time monitoring. For the latter, detection approaches are mainly based on the measurements of vibrations [13], strain [14] or elastic waves (vibro-acoustic emission) [15] on the blade. Since the sensors are required to be mounted inside the blade in advance, these detection approaches cannot be easily applied to in-service wind turbines. Other non-contact approaches based on infrared thermography cameras [16] or laser scanners [17] are potentially easier to apply to existing wind turbines. Similarly, the measurements of audible sound (20 Hz to 20 kHz) in the far-field or inside the blade structures with microphones can also be used as an alternative for blade damage detection [18–21]. Those airborne-sound-based methods can be classified into two basic categories: the active excitation method [22,23] and the passive excitation method [19,21]. The former relies on far-field measurements for acoustic waves, which are originally excited by the speakers inside the blade structures, passing through the holes or cracks of the blades. The latter places the microphones inside the blade structures to measure the flow-induced pressure responses due to the leakage of flow from the holes or cracks into the blade cavity. Besides the above two approaches using airborne sound, another possible acoustic solution for damage detection can be based on airfoil self-noise or turbulence-leading-edge impingement noise measurements in the far-field, of which the mechanisms of the sound generation are essentially different from the speaker-based or cavity-flow-responses induced ones. Compared with a clean blade, an eroded one usually has a rougher surface near the leading edge and a smaller thickness and radius at the leading edge due to the coating shedding [2,4,24]. These geometrical changes in airfoil shape and surface roughness may affect the noise generated aerodynamically both at the leading edge and trailing edge.

Previous studies, that have used aerodynamic noise measurements for damage detection [25–28], have been based on data-driven methods. However, the physical interpretation of the measured acoustic signal and the mechanism of the sound generation have not been investigated extensively nor related to the types and sizes of damage. Such data-driven models derived from existing databases may not be reliable when applied to new operating conditions, blade structures or damage severity. Several studies [29–31] have used a modified surface roughness to emulate blade erosion and assess its effect on the far-field noise. However, roughness tapes attached to airfoil surfaces cannot exactly mimic leading edge erosion, as in reality an eroded airfoil sees a reduced thickness as well as a roughened surface. Other numerical studies [32,33] have also investigated the effects of blade icing accretion on noise generation and far-field noise emission.

At low Reynolds numbers, i.e., at the blade inner radial locations, a laminar separation bubble may exist under clean inflow conditions. In this case, boundary layer instabilities in the form of Tollmien–Schlichting (T-S) waves can be triggered and an acoustic feedback loop can take place [34]. This phenomenon creates tonal noise known as laminar-boundary-layer–vortex-shedding noise [35–37]. The presence of small surface discontinuities due to erosion can affect the formation and development of the instabilities, thus causing different noise spectra in the far field. Furthermore, if the surface roughness or damaged region due to the erosion is large, the laminar separation bubble might not be present, and the boundary layer might develop directly into a fully turbulent one thus leading to broadband turbulent-boundary-layer-trailing-edge noise [29,38–40]. From a physical perspective, the damaged surface near the leading edge may force the boundary layer transition location to move towards the leading edge, thus affecting the turbulent boundary layer approaching the trailing edge and, as a consequence, affecting the spectra of the scattered turbulent-boundary-layer-trailing-edge noise.

In this study, we experimentally investigate the aerodynamic noise characteristics, with and without free-stream turbulence, when leading edge erosion occurs. A DU96 W180 airfoil with different leading edge erosion levels with pits, gouges and coating delamination scaled from a real eroded blade is tested in an anechoic wind tunnel. The aerodynamic noise scattered from the airfoil is measured and analyzed and a physical interpretation behind the acoustic data is postulated. Major differences between experiments carried out in a wind tunnel environment and real life are: the Reynolds number, often low in aeroacoustics facilities; and the presence of turbulence in the wind farm. Because of the former, an acoustic feedback loop might not be present in large wind turbines close to the tip of the blades, but only on the inner part of the blade. Considering the latter point, the presence of free-stream turbulence can cause turbulence leading edge impingement noise [41–44]. Previous studies revealed that there is a dependence between the wavelength of the free-stream turbulence, the leading edge radius and the thickness of the airfoil [41,45–50]. Furthermore, the effect of flow turbulence can potentially hinder the effect of leading edge erosion on transition, thus raising the possibility of assessing erosion from far-field noise measurements. For this reason, in this paper we also investigate this aspect, which is poorly analyzed in the literature so far.

The rest of the paper is organized as follows. In Section 2, the details of the facilities, test models and data processing configurations are presented. In Section 0, the results of acoustic measurements for different erosion levels are reported together with the physical interpretation of the noise generation mechanism. In this section the effects of erosion features, airfoil angle of attack and mean flow velocity on the noise spectra are discussed. The last section summarizes the findings from this study and proposes an outlook for future studies.

2. Experimental setup

2.1. Facilities and test models

Experiments were performed in the anechoic vertical open-jet tunnel (A-tunnel) of Delft University of Technology. The wind tunnel is equipped with a 40 cm × 70 cm rectangular test section, which allows a test with a maximum free-stream velocity of 45 m/s with turbulence intensity below 0.1%. The mean flow velocity non-uniformity within the whole test section is below 0.5% with respect to the velocity at the center [51]. The experimental setup is shown in Fig. 1.

Two grids (#1 and #2) were used to generate turbulence for moderate and high turbulence conditions. Inflow turbulence intensity and integral length scales with two grids mounted were measured using hotwire anemometry in a previous study [52] and are reported in Table 1.

A DU96 W180 airfoil was investigated. The profile of this airfoil was designed at Delft University of Technology for wind energy applications [53–55]. The airfoil model was made of aluminum by computer numerical control (CNC) machining (surface roughness: 0.05 mm) with a chord length, C, of 200 mm and span length, L, of 400 mm, as shown in Fig. 2. The leading edge is changeable which allows the testing of different erosion cases as well as a baseline (without any damage).

A global o-xyz Cartesian coordinate system is defined. The origin is located at the trailing edge mid-span of the airfoil. The x-axis is oriented with the direction of the free-stream, as shown in Fig. 1. An airfoil-based Cartesian reference system, O-XYZ, is also defined with origin at the trailing edge mid-span and X-axis oriented in the direction of the airfoil chord, as shown in Fig. 2.

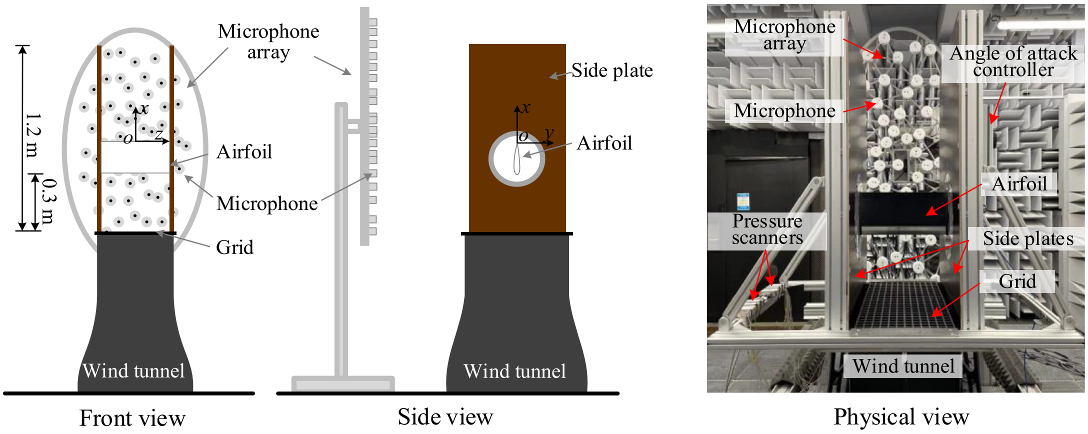

Fig. 1. Experimental setup.

Table 1
Turbulence intensity and integral length of the flow with grid mounted.

Grid No.	Turbulence intensity (%)	Turbulence integral length scale (mm)
#1	~ 4.0	7.9
#2	~ 7.1	10.2

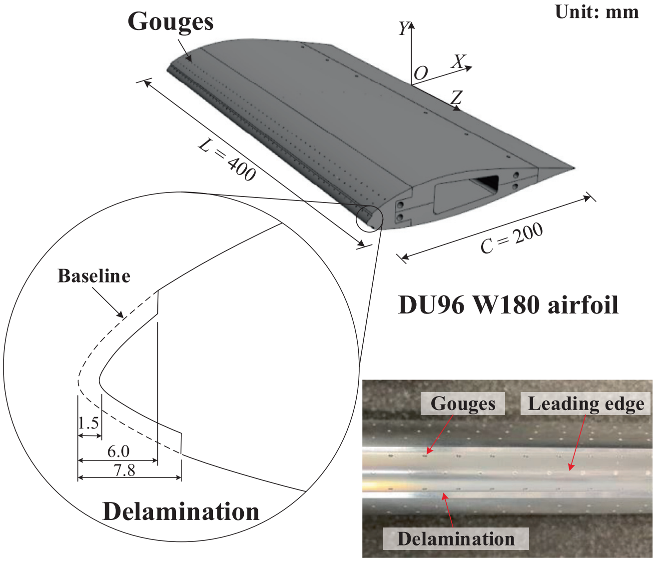

Fig. 2. Airfoil and leading edge erosion model: an example for damage level 4.

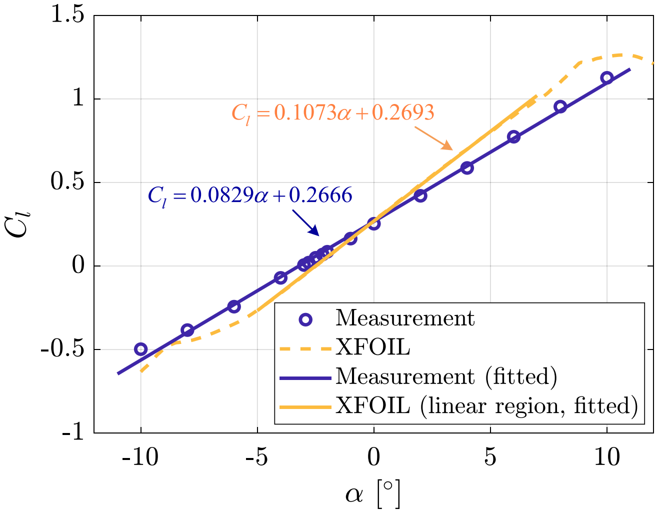

Fig. 3. Coefficient of lift versus angle of attack from measurement and XFOIL.

Due to the experiments being performed in an open test section, the effective angle of attack, α^*, of the airfoil is smaller than the geometrical angle of attack, α [35]. The effective angle of attack was obtained using the surface pressure distributions and compared with the data from XFOIL [56]. The static pressure was measured with two pressure scanners connected to sixteen pressure taps with 0.4 mm diameter on both pressure and suction side. The taps are distributed within the range of $-0.99 \leqslant X/C \leqslant -0.175$, tilted 15° to the airfoil centerline to avoid the contamination of the wakes from upstream taps on the downstream ones. The sampling frequency and accuracy of the pressure scanner are 100 Hz and 12.5 Pa, respectively. For each measurement, pressure data were recorded for 2 s. Fig. 3 shows the relationships between the calculated coefficient of lift, C_l, and the angle of attack from the measurement and XFOIL for 20 m/s free stream velocity. The correction factor, ξ, can be calculated from the slope ratio of the fitted curve from XFOIL to the one from the measurements, i.e., $\xi = 0.1073/0.0829 = 1.294$.

The design for the leading edge erosion is based on the measurements of eroded blades from 3 M [4] and the damage sizes are scaled to the airfoil used in this study. The leading edge erosion contains pits (P), gouges (G) and coating delamination (DL). The simulated pits (with depth and diameter of 0.2 mm) and gouges (with depth and diameter of 1.0 mm) are simplified as hollow cylinders and the coating delamination is simulated as a sunken offset with 1.5 mm depth to the baseline surface at the leading edge. The pits and gouges are staggered and distributed within $-200\text{ mm} \leqslant X \leqslant -180\text{ mm}$ on the suction side and $-200\text{ mm} \leqslant X \leqslant -174\text{ mm}$ on the pressure side, respectively. The chordwise extension ranges of the coating delamination are from the leading edge up to 2, 4, and 6 mm on the suction side and 2.6, 5.2, and 7.8 mm on the pressure side for different delamination severities (DL, DL + and DL++). The distributed range of damage features on the pressure side is 1.3 times the one on the suction side, as suggested in [4], which takes into account that the pressure side of a real blade is vulnerable to more severe erosion. The detailed dimensions and distributed range of the erosion features are shown in Table 2.

Four erosion levels are designed with different combinations of erosion features. Table 3 shows the amounts of pits or gouges and

Table 2
Dimensions and distributed range of erosion features.

Features	Depth/ Dimeter (mm)	Damaged range (mm)	
		Pressure side	Suction side
Pits (P)	0.2 (0.1% C)	26 (13% C)	20 (10% C)
Gouges (G)	1.0 (0.5% C)	26 (13% C)	20 (10% C)
Delamination (DL)	1.5 (0.75% C), depth	2.6, 5.2, 7.8 (1.3%, 2.6%, 3.9% C) for DL, DL+, DL++	2, 4, 6 (1.0%, 2.0%, 3.0% C) for DL, DL+, DL++

the severity of delamination for different damage levels. Considering the fact that the scaled dimension of the pits is far smaller than gouges and delamination, the effect of those pits on aerodynamic noise emission will be negligible, thus the pits were not manufactured for the simulated erosion cases (Level 1 $\sim$ 4). Alternatively, in order to investigate the separate influence of the pits, gouges and delamination on the noise emission, three additional leading edge parts with a single type of erosion feature were manufactured. In Fig. 2, an example of the geometry and real test leading edge of damage level 4 is shown.

2.2. Phased microphone array and acoustic measurements

Far-field noise was measured using a 2-D planar phased microphone array which contained 64 *G.R.A.S. 40PH* free-field microphones. The microphone array was placed at $y = -1$ m, as shown in Fig. 1. The distribution of the microphones in the array is shown in Fig. 4. The reference microphone was set at (0.2, 0, -1) m to ensure all microphones being out of the acoustic shadow of the wind tunnel nozzle. The frequency response of the microphone is within ±1 dB between 50 Hz and 5 kHz, and within ±2 dB between 5 kHz and 20 kHz. The maximum measurable range of the microphone is 135 dB with respect to the reference pressure of 20 μPa.

The acoustic signal of each test case was recorded for 20 s with a sampling frequency, f_s, of 51.2 kHz. For each measurement, the signal was separated into time chunks of 5120 samples with 50% data overlap for the Fourier transform. For each chunk, a Hanning weighting function was applied to reduce the energy leakage. The cross-spectral matrix was averaged from the obtained auto spectra of the Fourier transform. Conventional frequency domain beamforming (CFDB) [57–61] was performed on a square scan plane parallel to the xoz plane, ranging: $-0.5\text{ m} \leqslant x \leqslant 0.5\text{ m}$ and $-0.5\text{ m} \leqslant z \leqslant 0.5\text{ m}$. The distance between the microphone array and scan plane was corrected with the airfoil angle of attack (at non-zero). The background noise from the wind tunnel test section and turbulence generating grids was measured under the same test condition before the airfoil is mounted. Then the background noise was reduced by means of the eigenvalue identification and subtraction (EIS) algorithm reported in [61]. A source power integration (SPI) technique [62,63] was applied within a rectangular box (as shown in Fig. 4) with a size of 10 cm × 20 cm centered at the midpoint of the leading edge or trailing edge to look at the noise scattered from the regions of interest.

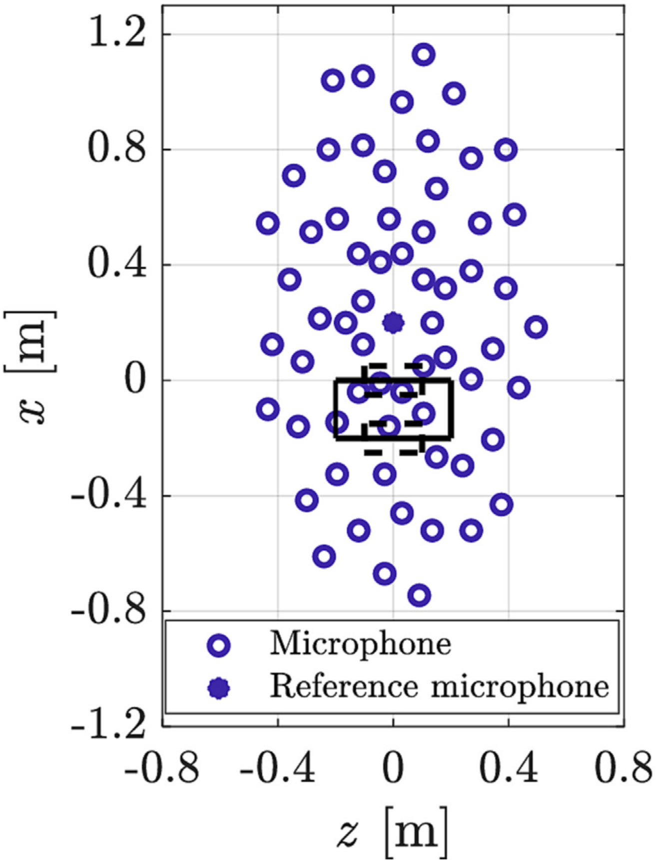

Fig. 4. Microphones in the array. The solid box is the projection of the airfoil onto the array plane and the top or bottom dashed box is the corresponding source power integration region at the leading edge or trailing edge, respectively.

The noise spectrum in this study is quantified using the sound pressure level (SPL) which is defined as:

$$L_p = 10\lg\left(\frac{p_e^2}{p_{ref}^2}\right) \tag{1}$$

where p_e is the root mean square sound pressure fluctuations and p_{ref} is the reference pressure, 20 μPa in air.

2.3. Surface oil flow visualization

To investigate the effect of erosion on flow transition on the airfoil surfaces, surface oil flow visualization [64] was carried out. The setup is shown in Fig. 5(a). A fluorescing oil mixture was made of paraffin oil and petroleum. The mixture was brushed on the airfoil

Table 3
Leading edge erosion design for different damage levels.

Damage case			Erosion features	
No.	Description		Pressure side	Suction side
0	Baseline		–	–
1	Simulated erosion	Level 1	30 G	25 G
2		Level 2	65 G / DL	50 G / DL
3		Level 3	130 G / DL+	100 G / DL+
4		Level 4	260 G / DL++	200 G / DL++
5	Decoupled features from level 4		520P	400P
6			260 G	200 G
7			DL++	DL++

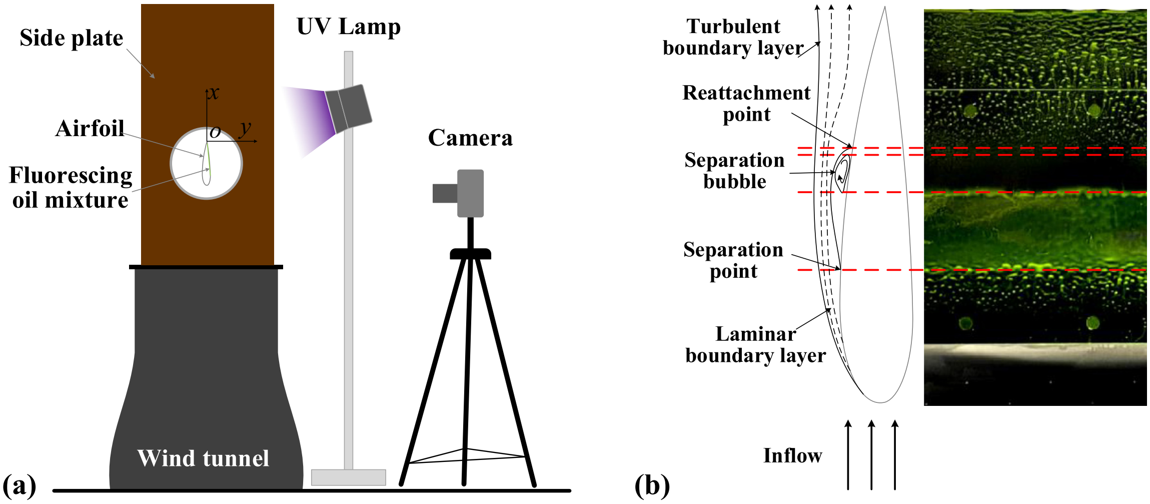

Fig. 5. Setup of surface oil flow visualization: (a) a sketch; (b) an example and interpretation for oil visualization of damage level 2 under clean flow condition with a mean flow velocity of 30 m/s (picture was taken on the suction side at an angle of attack of 0°).

surface and then fluorescence was excited with an ultra-violet (UV) lamp. Pictures were taken by a digital camera. The distribution of this oil film was affected by shear forces and the change in the velocity gradient of flow, induced by a laminar or turbulent boundary layers or other features. As an example, flow separation is visualized [65,66] in Fig. 5(b).

2.4. Test conditions

The experiments were carried out under five different mean flow velocities. The mean flow velocity and relevant chord-length-based Reynold numbers ($Re_C = \bar{U}C/\nu$, where ν is kinematic viscosity) are shown in Table 4. For each mean flow velocity, three inflow conditions were tested: clean inflow and turbulent inflow obtained by mounting one of two different grids.

Five angles of attack were selected to investigate the effect of the airfoil angle of attack on the ability to detect erosion under zero lift, zero angle of attack, low angle of attack, pre-stall and stall conditions. The geometrical angles of attack and the corresponding effective ones are listed in Table 5.

3. Results and discussion

3.1. Identification of erosion level

3.1.1. Clean inflow condition

Fig. 6 shows the spectra of sound pressure level at the trailing edge measured with the microphone array facing both the suction and pressure side for different damage levels for the clean inflow case. The angle of attack is 0°, the free-stream velocity 30 m/s. When there is no damage (baseline) or the damage is small (e.g., damage level 1), at a low Reynolds number, laminar boundary layer instability noise can be observed. The noise spectra typically show the combination of a broadband hump with a series of tonal peaks [34,67–70]. Both on the suction and pressure side, the broadband contributions of the damage level 1 do not show many differences compared with the baseline case, both in amplitude and frequency. However, on the suction side, the amplitude of the tones for damage level 1 is larger than that for the baseline. For example, the amplitudes of the dominant tones are 48.36 dB ($f_{n,\max}$ at 1800 Hz) for damage level 1 and 41.25 dB ($f_{n,\max}$ at 1830 Hz) for the baseline case, respectively. This is attributed to a change in the size of the laminar separation bubble, which becomes longer on the suction side with respect to the baseline case. This is confirmed by the surface oil flow visualization technique shown in Fig. 7. On the suction side, since the separation bubble is larger and closer to the trailing edge, more coherent vortices are shed near the trailing edge, thus resulting in larger tonal noise [37,71–73]. Fig. 6 also shows the spectra normalized by chord-length-based Strouhal number, St_C. For the damage level 1 case, the dominant tone occurs at $St_C = 12.0$ on the suction side and $St_C = 10.2$ on the pressure side and the baseline cases at $St_C = 12.2$ and $St_C = 10.2$, respectively. The frequency of the dominant tones does not change in the presence of a small amount of damage. For the baseline case, there is also a secondary harmonic tone on the suction side at $St_C = 5.9$, while, for the damage level 1 case, there is not. Similar results are reported in [71], where the tones on the suction side and pressure side lock on to the same frequency (and the same St_C) for the NACA 0012 airfoil. The asymmetry of the DU96 W180 airfoil may be responsible for the difference (i.e., a smaller peak St_C on the pressure side) between the results of this study and in [71].

When the damage becomes larger, for example damage level 2, on the pressure side, the flow is turbulent right after the eroded region as shown in Fig. 7, thus resulting in broadband far-field noise as shown in Fig. 6. A small tone appears at $St_C = 15.7$ and might be due to the noise scattered from the feedback loop present on the suction side. On the suction side, a similar spectral shape to the damage 1 case is found. The major difference is that the amplitude is lower and both the broadband hump and the tonal peaks shift to a higher frequency region. As a matter of fact, the dominant tone is found at $St_C = 15.7$ for the damage level 2 case, while it is at $St_C = 12.2$ for the damage level 1 case. Previous studies observed similar trends when forcing transition on the pressure side [71,74].

When the damage level becomes even larger (e.g., damage levels 3 and 4), the spectra both on the suction and pressure side show only broadband features (Fig. 6). Surface oil flow visualization results of those cases, as shown in Fig. 7, confirm that the boundary layer is turbulent on both sides. However, when comparing the spectra, the overall trend is that as the damage level is larger, there is an energy increase in the low-frequency range and a decrease in the high-frequency one. The potential cause for this spectral shape is that a larger damage area leads to more large-scale turbulence structures and a thicker boundary layer at the trailing edge; as a result, the energy is redistributed to a lower frequency region.

Table 4
Test conditions of mean flow velocities and Reynold numbers.

No.	1	2	3	4	5
$\bar{U}$(m/s)	15	20	25	30	35
Re_C	2.0×10^5	2.7×10^5	3.4×10^5	4.1×10^5	4.7×10^5

Table 5
The angles of attack tested in the experiment.

No.	1 ($C_l = 0$)	2 ($\alpha = 0^\circ$)	3 (low)	4 (pre-stall)	5 (stall)
$\alpha(^\circ)$	−3.2	0	5	10	15
$\alpha^*(^\circ)$	−2.5	0	3.8	7.7	11.6

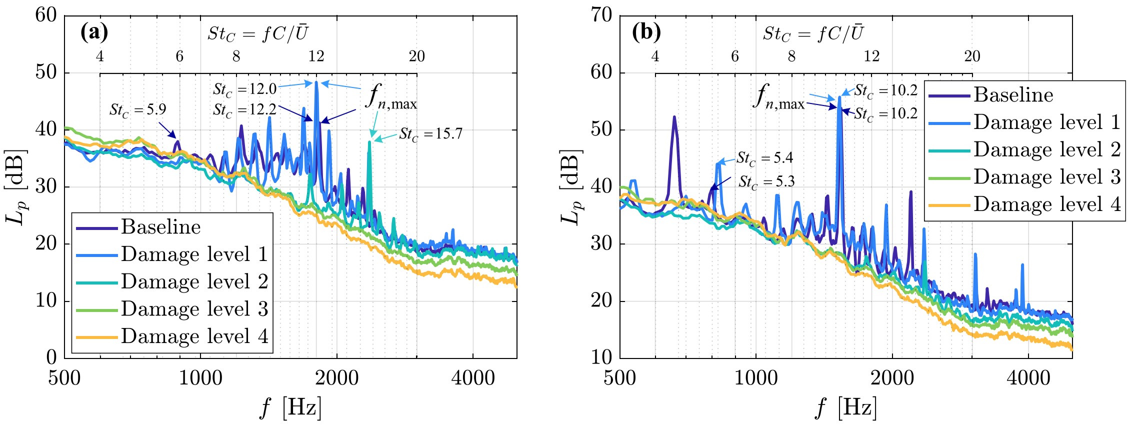

Fig. 6. Spectra of sound pressure level at tailing edge for different damage levels at the angle of attack of 0° under clean flow condition with the mean flow velocity of 30 m/s: (a) on the suction side and (b) on the pressure side.

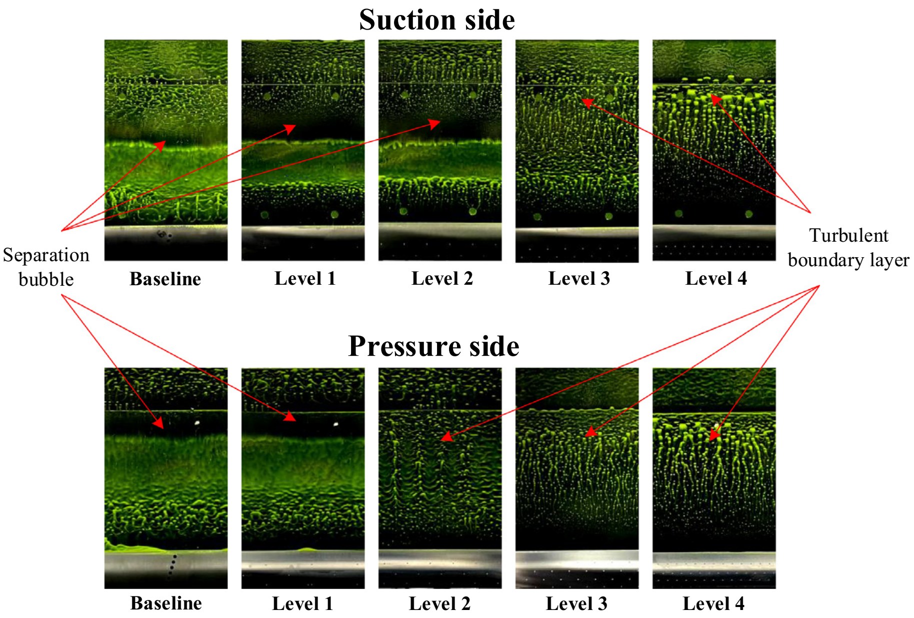

Fig. 7. Surface oil flow visualization for different damage levels at the angle of attack of 0° under a clean flow condition with the mean flow velocity of 30 m/s.

3.1.2. Turbulent inflow conditions

In presence of a turbulent inflow, as shown by the beamforming maps in Fig. 8, three different noise sources can be identified: one from the grid, one from the airfoil leading edge and one from the trailing edge. The noise generated by the grid strongly increases the background noise, thus affecting the quality of the measurement. To reduce the contribution from the grid, the signal processing approach discussed in Section 2.2 has been applied. Furthermore, data are presented only below 2000 Hz to keep a high ratio of airfoil noise to grid background noise.

Fig. 9 shows the sound pressure level at the trailing edge for different damage cases as well as the baseline when grid #1 is

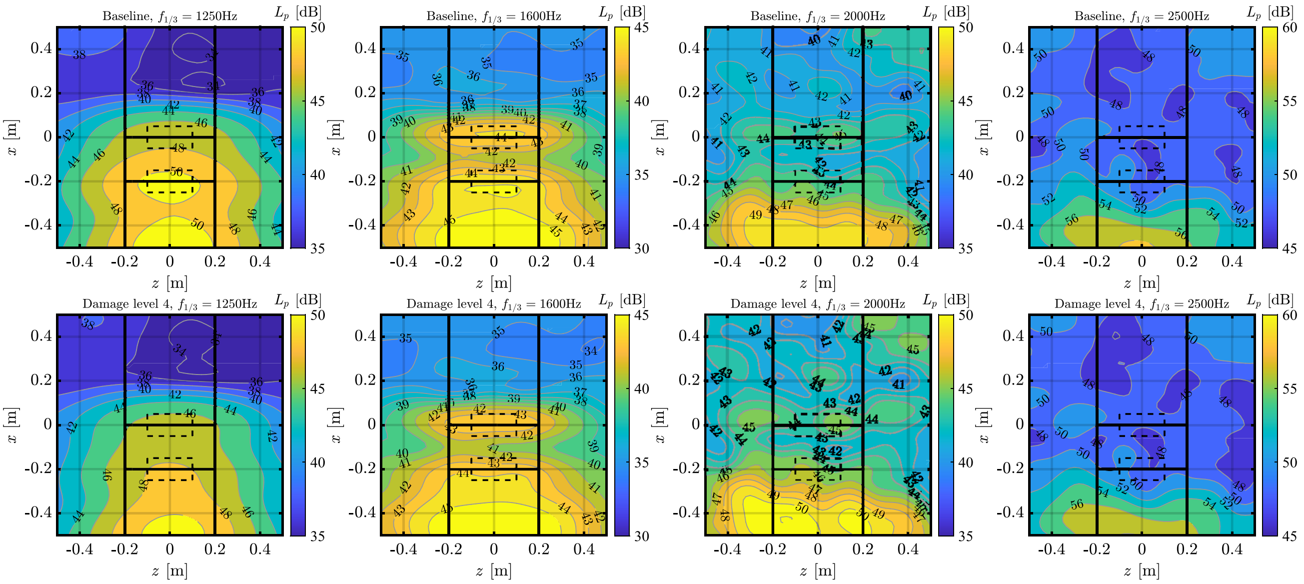

Fig. 8. Beamforming maps on the suction side at one-third octave central frequency from 1250 Hz to 2500 Hz with grid #1 mounted when the flow velocity is 30 m/s at 0° angle of attack for baseline and damage level 4.

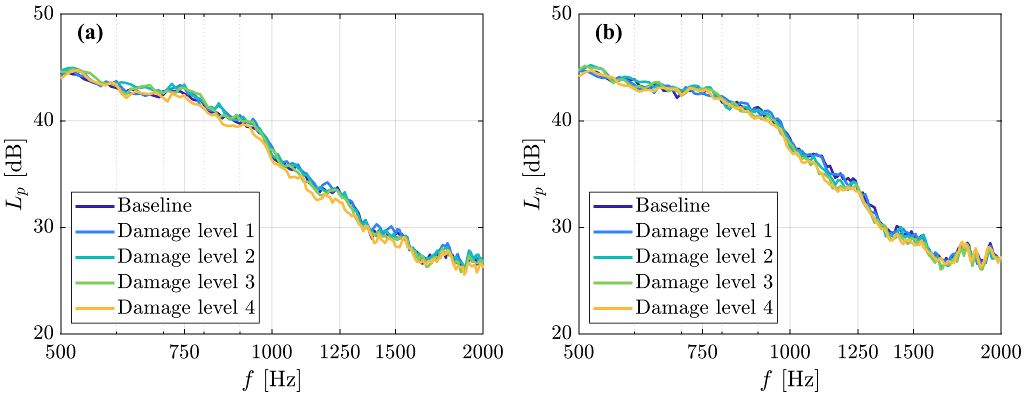

Fig. 9. Spectra of sound pressure level at the trailing edge for different damage levels at an angle of attack of 0° when grid #1 is mounted with a mean flow velocity of 30 m/s: (a) on the suction side and (b) on the pressure side.

mounted for the mean flow velocity of 30 m/s and airfoil angle of attack of 0°. Due to the turbulent inflow, the boundary layer transition to turbulent very close to the leading edge, as shown in Fig. 10. Therefore, the noise scattered from the trailing edge can be attributed to the trailing edge turbulent boundary layer noise mechanism. However, in this condition, for all the presented cases, there is no difference between the far-field noise generated at the trailing edge. This means that damage detection using the trailing edge noise is not a valid approach.

At the leading edge, where turbulent inflow impingement noise occurs, the noise spectrum presents a decaying trend above 1000 Hz both on the pressure and suction side when the damage level increases, as shown in Fig. 11 (a) and (b). Fig. 11 (c) and (d) show the relative spectral differences from the baseline, $\Delta L_p = L_{p,\text{Baseline}} - L_{p,\text{Damage}}$, against chord-length-based Strouhal number St_C. The spectral difference shows a hump with increasing amplitude as the damage level increases. The frequency at which the hump reaches its maximum is nearly constant for all the cases at $St_C \sim 10$. Previous studies [41,50,75] focusing on the effects of leading edge radius and airfoil thickness on the turbulent inflow impingement noise, attributed the reduction in the high-frequency range to the larger distortion of the turbulent velocity in the larger stagnation region [41], because the distortion of the turbulent structures is related to the slope angle of the steady mean flow near the leading edge. To confirm this, a 2-D RANS numerical calculation is performed using Ansys Fluent CFD software platform. The standard k-ε two-equation turbulence model is used in the simulation providing a reasonable compromise between calculation speed and accuracy. Fig. 12 shows numerical results for the mean velocity around the leading edge for baseline and damage level 4 under the same condition as in the experiments. The region where the mean velocity is lower than 80% of inflow velocity is determined as the stagnation region. The result shows that for the damage level 4 case, there is a larger stagnation region with larger mean flow curvature compared with the baseline, particularly due to the steps introduced to mimic the erosion damage under investigation.

Fig. 13 presents the spectra of sound pressure level when grid #2 is mounted, where the turbulence intensity is at ~7.1%. Similar results to the previous case can be observed but the spectral differences between those cases become smaller. This means the turbulent inflow with high turbulence intensity may reduce the

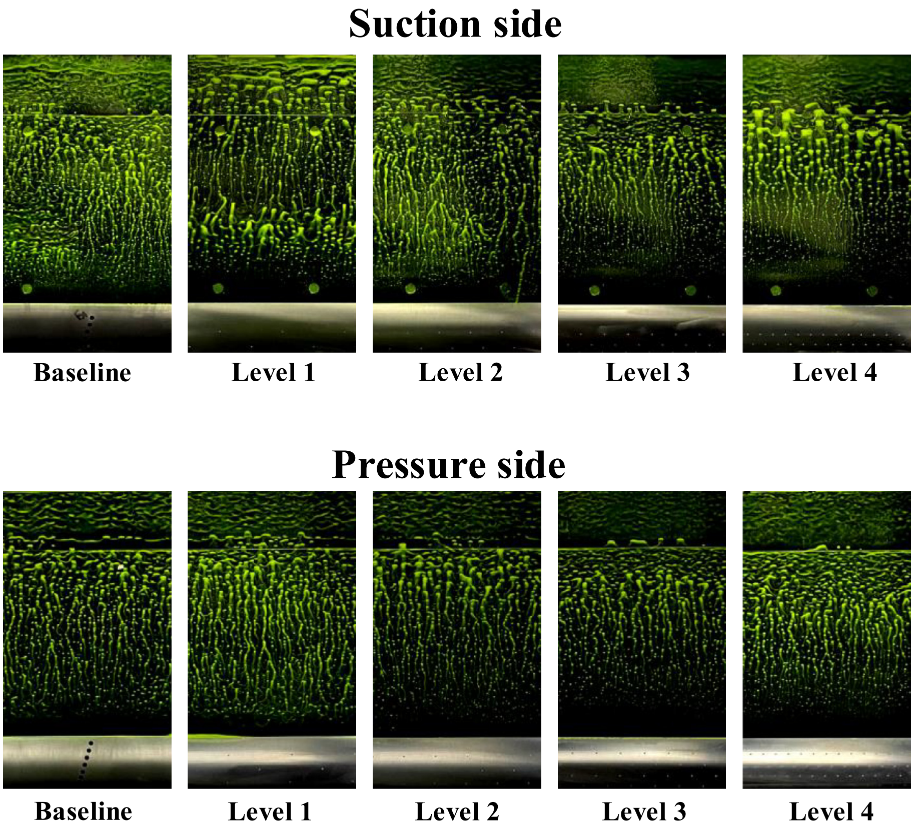

Fig. 10. Surface oil flow visualization for different damage levels at an angle of attack of 0° when grid #1 is mounted with a mean flow velocity of 30 m/s.

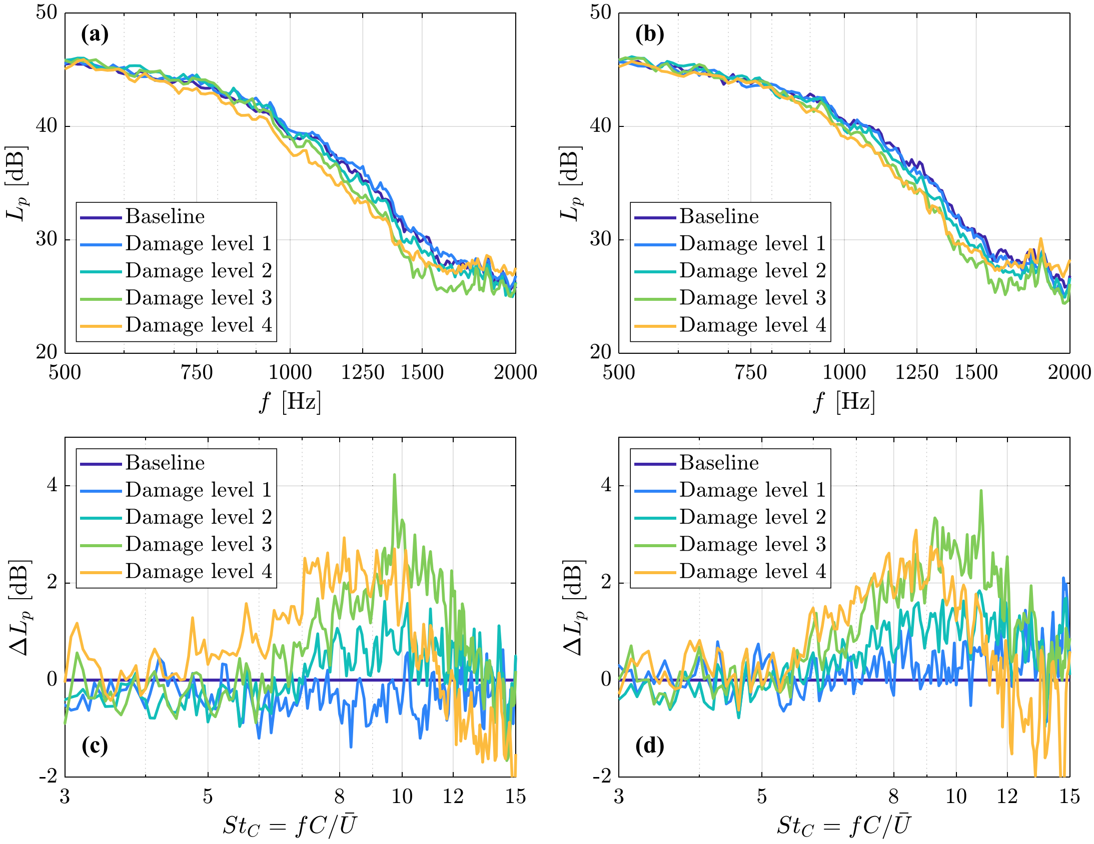

Fig. 11. Spectra of sound pressure level and spectral differences compared to the baseline at the leading edge for different damage levels at an angle of attack of 0° when grid #1 is mounted with a mean flow velocity of 30 m/s: (a), (c) on the suction side and (b), (d) on the pressure side.

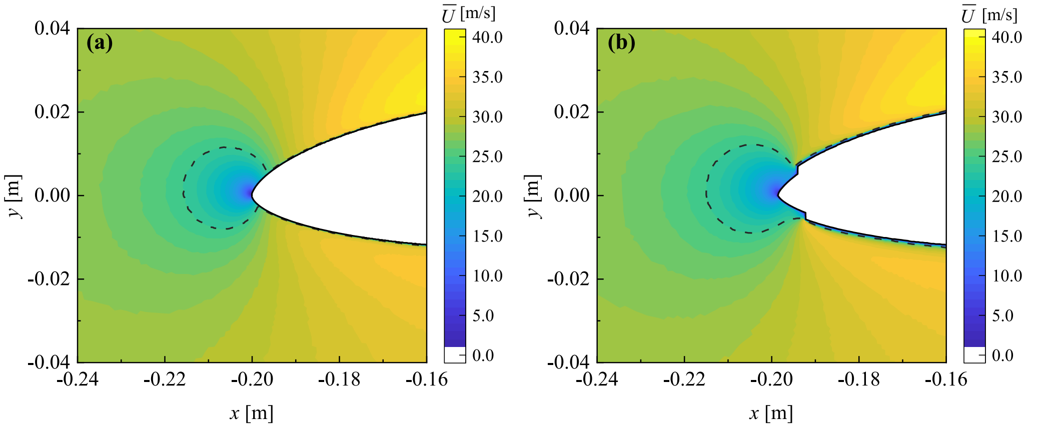

Fig. 12. Mean velocity around the leading edge for baseline and damage level 4 at the angle of attack of 0° under inflow mean velocity of 30 m/s with grid #1 mounted: (a) baseline and (b) damage level 4. The region bounded by the dashed line is below 80% inflow mean velocity, i.e., 24 m/s, representing the stagnation region.

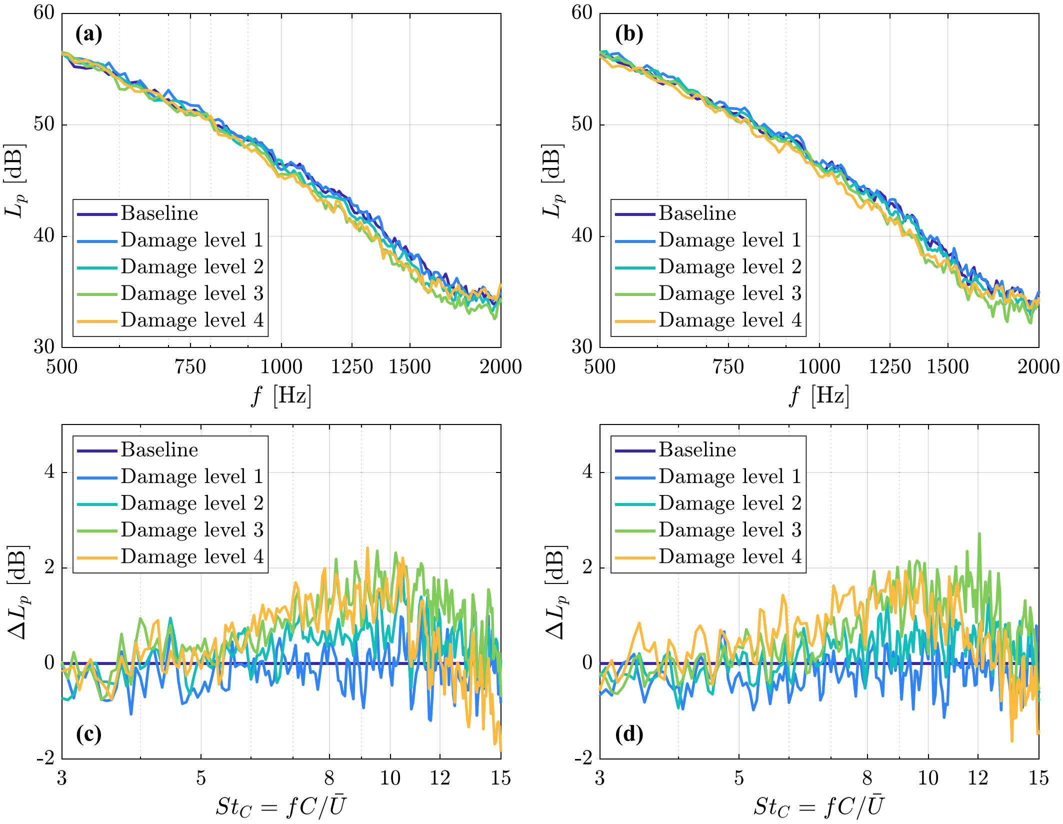

Fig. 13. Spectra of sound pressure level and spectral differences to the baseline at the leading edge for different damage levels at the angle of attack of 0° when grid #2 is mounted with the mean flow velocity of 30 m/s: (a), (c) on the suction side and (b), (d) on the pressure side.

sensitivity for damage detection by analyzing the spectra of leading edge noise.

3.2. Effect of erosion features

The eroded leading edge investigated contains three features: pits, gouges, and delamination. In this section, we take erosion level 4 as an example to investigate the effect of different erosion features on the far-field noise. In Fig. 14, the spectra of the trailing edge noise for each of the isolated features present in case 4 are investigated under clean inflow conditions. The spectra of the cases with pits and gouges show laminar boundary layer instability noise characteristics. On the suction side, the discrete tones caused by the gouges case are significantly higher than the one measured for the baseline and pits-only cases; as a matter of fact, the dominant tones for the cases of gouges, pits and baseline are 56.66 dB, 45.49 dB and 41.25 dB, respectively. Conversely, on the pressure side, no clear trend is observed. The spectra of the delamination case on the suction side and pressure side are essentially consistent with the ones of damage level 4.

In Fig. 15, the spectra for the leading edge noise under the turbulent inflow conditions (with grid #1 mounted) are shown. The

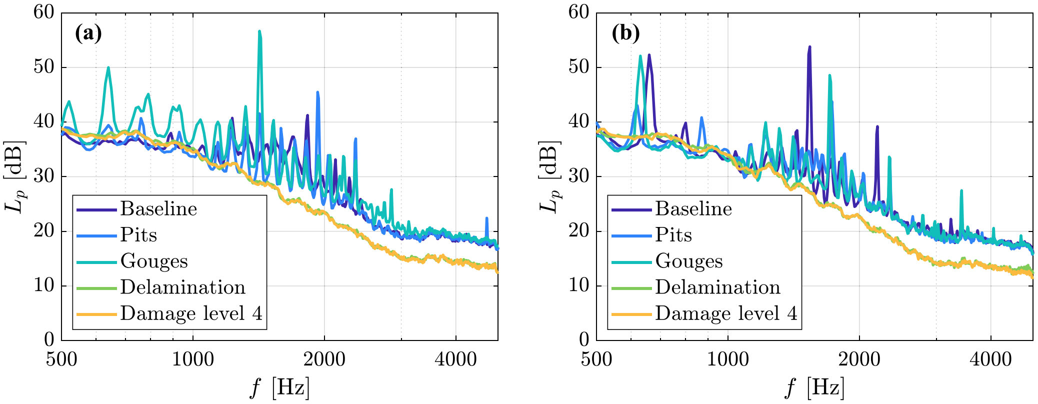

Fig. 14. Spectra of sound pressure level at trailing edge for baseline, damage level 4 and its different erosion features at angle of attack of 0° under clean flow condition with mean flow velocity of 30 m/s: (a) on suction side; (b) on pressure side.

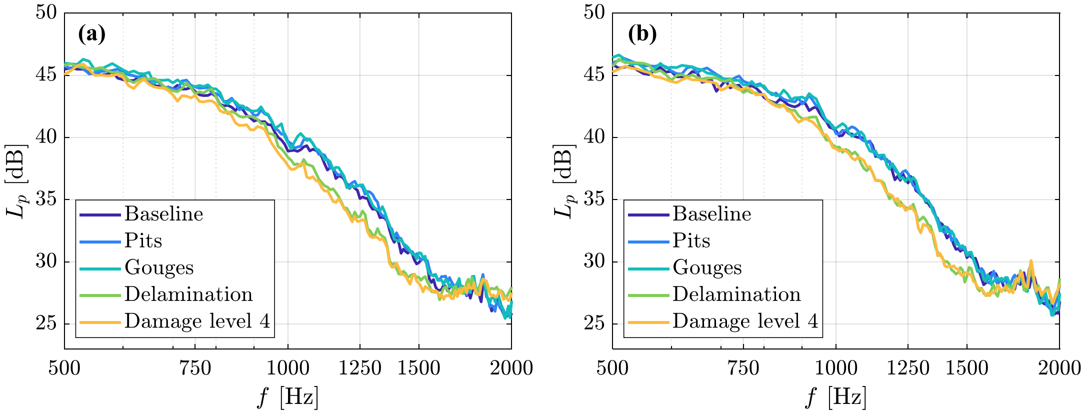

Fig. 15. Spectra of sound pressure level at the leading edge for baseline, damage level 4 and its different erosion features at an angle of attack of 0° under mean flow velocity of 30 m/s with grid #1 mounted: (a) on the suction side; (b) on the pressure side.

spectra of cases of pits and gouges almost coincide with the baseline while the spectra of the delamination case tend to the ones of damage level 4, in agreement with the physical explanation provided in the previous section. This suggests that both under clean and turbulent conditions, the delamination feature of the erosion dominates the nature of the noise spectra.

3.3. Effect of airfoil angle of attack

In Fig. 16, the spectra of sound pressure level for the trailing edge noise under a clean inflow condition for the damage level 4 case and the baseline case at different angles of attack are shown. For the baseline configuration, at a low ($\alpha = -3.2^\circ,\ 0^\circ,\ 5^\circ$) or moderate ($\alpha = 10^\circ$, pre-stall) angle of attack, the spectra are characterized by laminar boundary layer instability noise. The tonal components are enhanced with increasing angle of attack both on the suction and pressure side. For the highest angle of attack investigated ($\alpha = 15^\circ$, stall), where the airfoil is operating under stall conditions, the far-field noise spectra show broadband features with an increase of noise in the low frequency range with respect to other angles of attack. This is caused by the large vortices present in the separated boundary layer. By contrast, for the case of damage level 4, when the airfoil is at a low ($\alpha = -3.2^\circ,\ 0^\circ,\ 5^\circ$) and moderate ($\alpha = 10^\circ$) angle of attack, the spectra show broadband turbulent boundary layer noise characteristics, similarly to what was observed in the previous section. Moreover, on both the suction side and pressure side, the intensity of noise in the low-frequency range increases while it decreases in the high-frequency range as the angle of attack increases. In contrast to the baseline case, when the airfoil is at $\alpha = 15^\circ$, the spectra for the damaged case show higher noise intensity in the low frequency region and lower noise intensity in the high frequency region compared with the baseline case.

When turbulent inflow is introduced, the noise from the leading edge rather than the trailing edge contains the effective information for the identification of damage as discussed before. In this case, the spectra of the leading edge noise are discussed under turbulent inflow conditions. With grid #1 mounted, as shown in Fig. 17, the variation in the angle of attack does not affect the leading edge impingement noise under low and moderate angles of attack ($\alpha = -3.2^\circ,\ 0^\circ,\ 5^\circ,\ 10^\circ$) for both the baseline and damage level 4 cases. By comparing the two configurations for these angles of attack, it is evident that above 1000 Hz, the sound levels of the damaged cases are consistently lower compared with those of the baseline, independent of the angle of attack. However, for a stall condition, this trend is opposite. The above results suggest that the change in the angle of attack does not affect the ability to recognize damage and the proposed approach is valid under a wide range of airfoil angles of attack.

3.4. Effect of mean flow velocity

Fig. 18(a) and (b) show the sound pressure level of trailing edge noise under a clean inflow condition with different velocities for damage level 4. The spectra of the noise for both sides are broadband under these testing velocities. Fig. 18(c) presents the overall

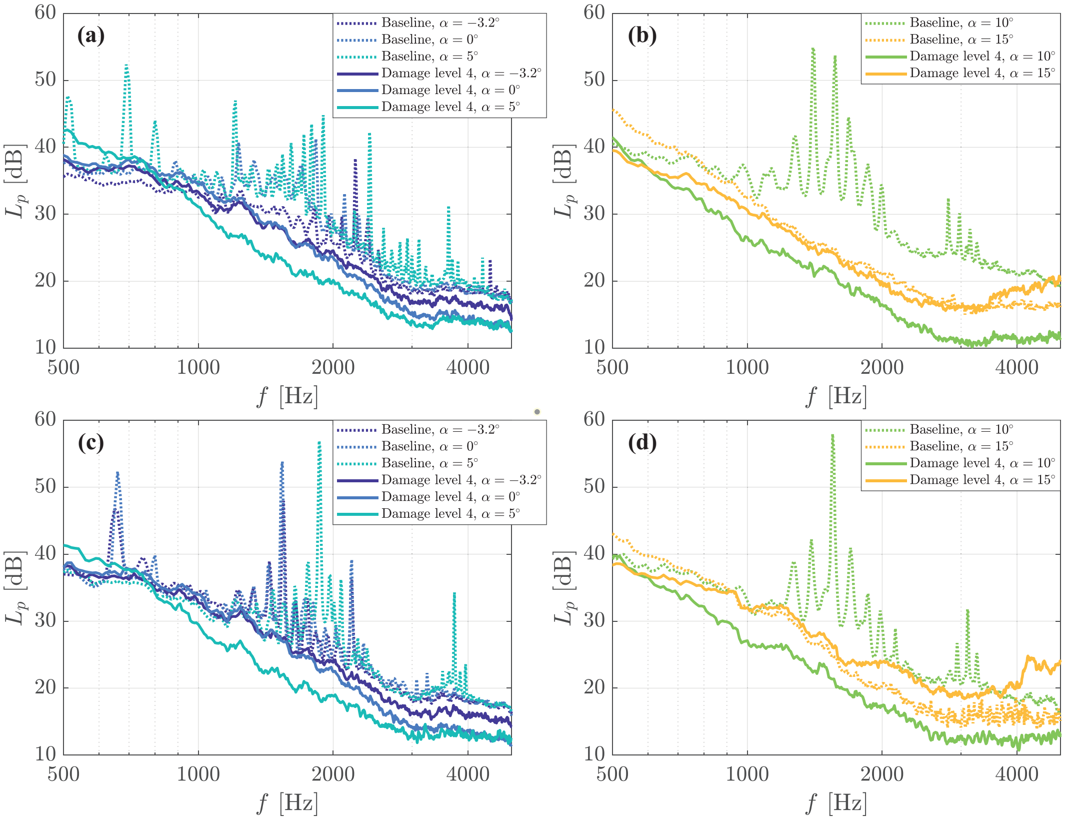

Fig. 16. Spectra of sound pressure level of trailing edge noise for different angles of attack under clean flow condition with inflow velocity of 30 m/s: (a) and (b) on the suction side; (c) and (d) on the pressure side.

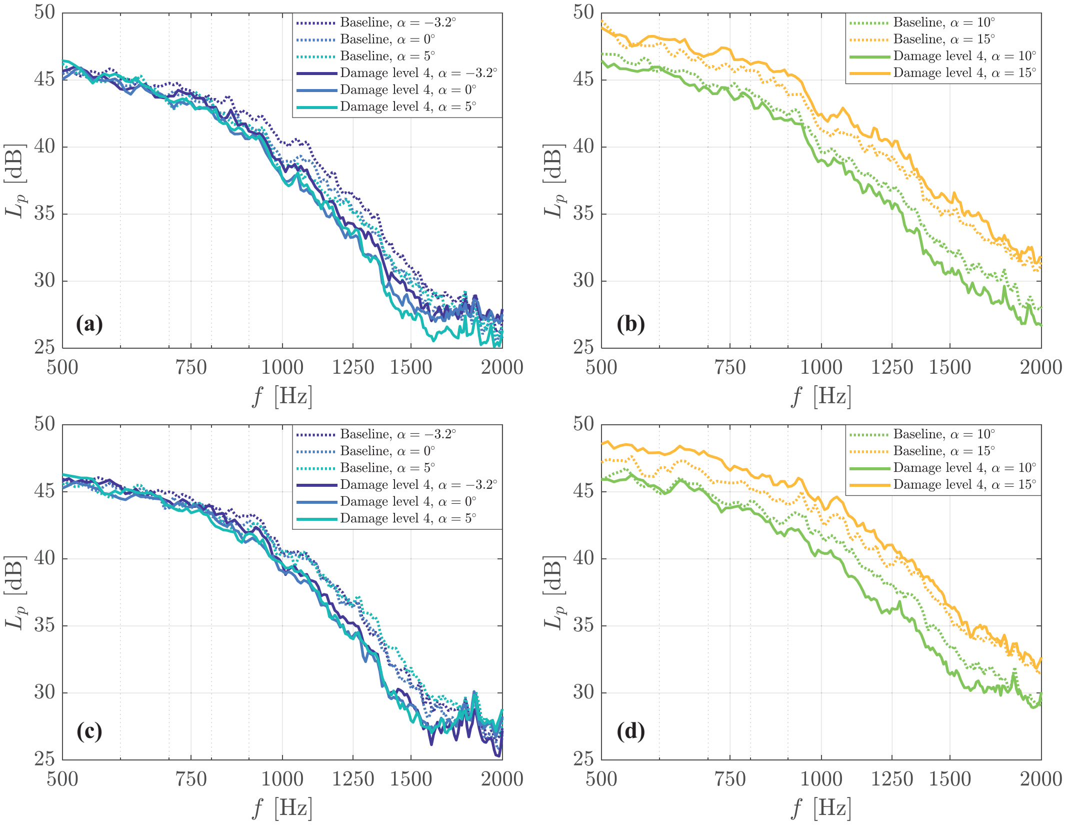

Fig. 17. Spectra of sound pressure level of leading edge noise for different angles of attack under turbulent flow condition with grid #1 mounted and mean flow velocity of 30 m/s: (a) and (b) on the suction side; (c) and (d) on the pressure side.

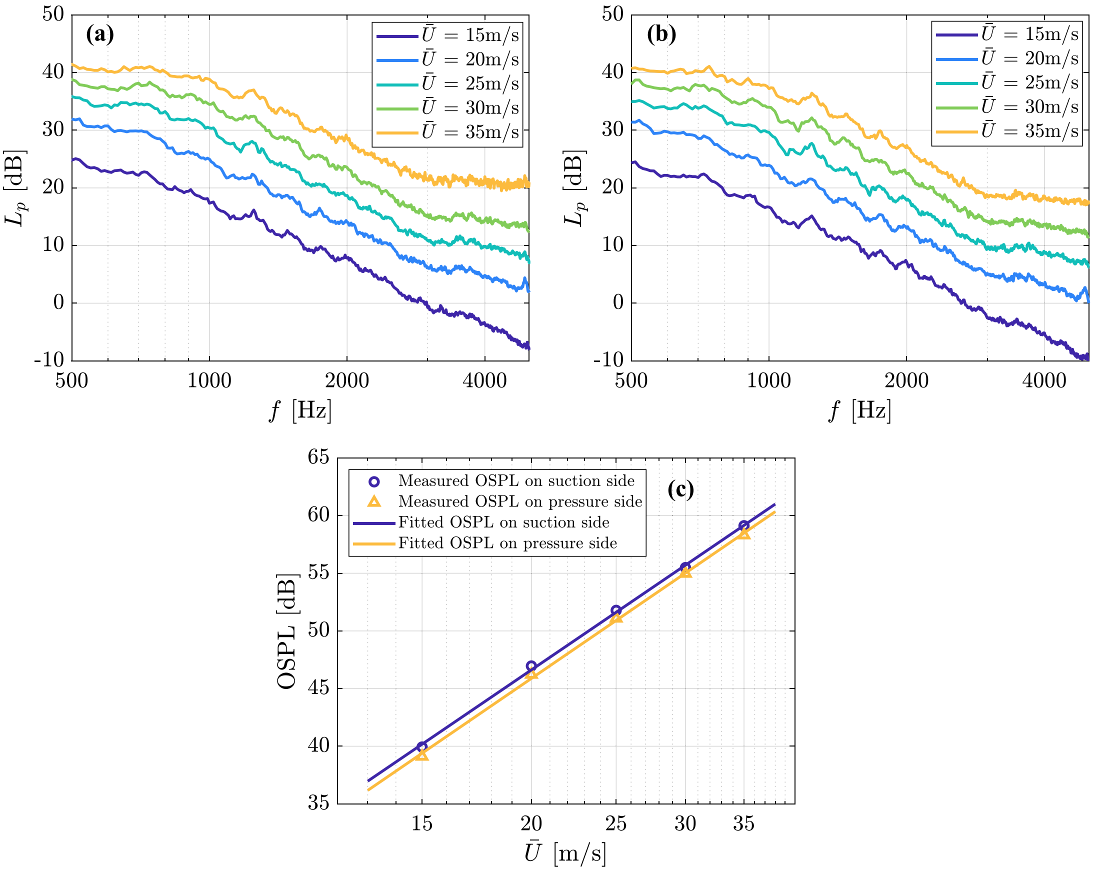

Fig. 18. Sound pressure level of trailing edge noise for damage level 4 under clean inflow condition with different velocities at the angle of attack of 0°: (a) spectra on the suction side; (b) spectra on the pressure side; (c) overall sound pressure level to mean flow velocity.

sound pressure level (OSPL) against the flow velocities. The OSPL is integrated between 500 Hz and 5000 Hz. As expected, the OSPL shows an approximate fifth power law of velocity dependency (5.16 and 5.19 on suction and pressure sides, respectively). This is consistent with previous studies on turbulent boundary layer trailing edge noise [31,35,76].

When inflow is turbulent, the spectral features of leading edge impingement noise can be used for damage detection. Fig. 19 shows the spectra of the leading edge impingement noise for damage level 4 and baseline as well as their spectral differences (i.e., $\Delta L_p = L_{p,\text{Basline}} - L_{p,\text{Damage}}$) under different mean flow velocities when grid #1 is mounted. Compared with the baseline, in Fig. 19 (a) and (b), the spectrum of the damage level 4 is lower within a specific band under a given velocity. Moreover, the region with lower noise intensity shifts to high frequency as the mean flow velocity increases. When normalizing the frequency as chord-length-based Strouhal number, the peaks of ΔL_p are all approximately at $St_C \sim 10$, which suggests a proportional relation between the spectral features and the velocity. Moreover, when looking at the amplitudes of ΔL_p, the change in velocity does not affect the detection sensitivity.

4. Conclusions

In this study, the aerodynamic noise of a DU96 W180 airfoil with leading edge erosion was investigated for the purpose of the development of a non-contact approach for damage detection and condition monitoring for wind turbine blades. The experimental results showed that it is possible to use the spectral features of trailing edge noise under a clean flow condition and leading edge noise under turbulent conditions for erosion damage detection.

Under a clean inflow condition and low Reynolds number, when the damage level is minor (e.g., damage level 1), the frequencies of the tones do not change while the amplitude becomes higher than those of the baseline case. When at a moderate damage level (damage level 2), the tones can only be found from noise spectra on the suction side, and they shift to a higher frequency region with lower amplitudes. Furthermore, when the damage level is larger (damage levels 3 and 4), the noise scattered from the trailing edge becomes broadband and as the damage level increases the low-frequency contributions increase while the high-frequency contributions decrease.

Under turbulent inflow conditions, however, the spectra of the trailing edge noise for different damage cases are almost the same. This suggests that it is invalid to use the trailing edge noise for leading edge erosion detection. As the damage level increases, mid-high frequency contributions of the leading edge impingement noise decreases. This is because a greater level of erosion leads to a larger distortion of the incoming turbulent eddies. When the turbulence intensity increases, the differences in impingement noise between the different damage levels become smaller which suggests that for a high turbulence condition the detection may be affected.

The effects of erosion features, airfoil angle of attack and mean flow velocity were also investigated. By comparing spectral results of each isolated erosion feature at damage level 4 (pits, gouges and coating delamination) and the baseline, it is found

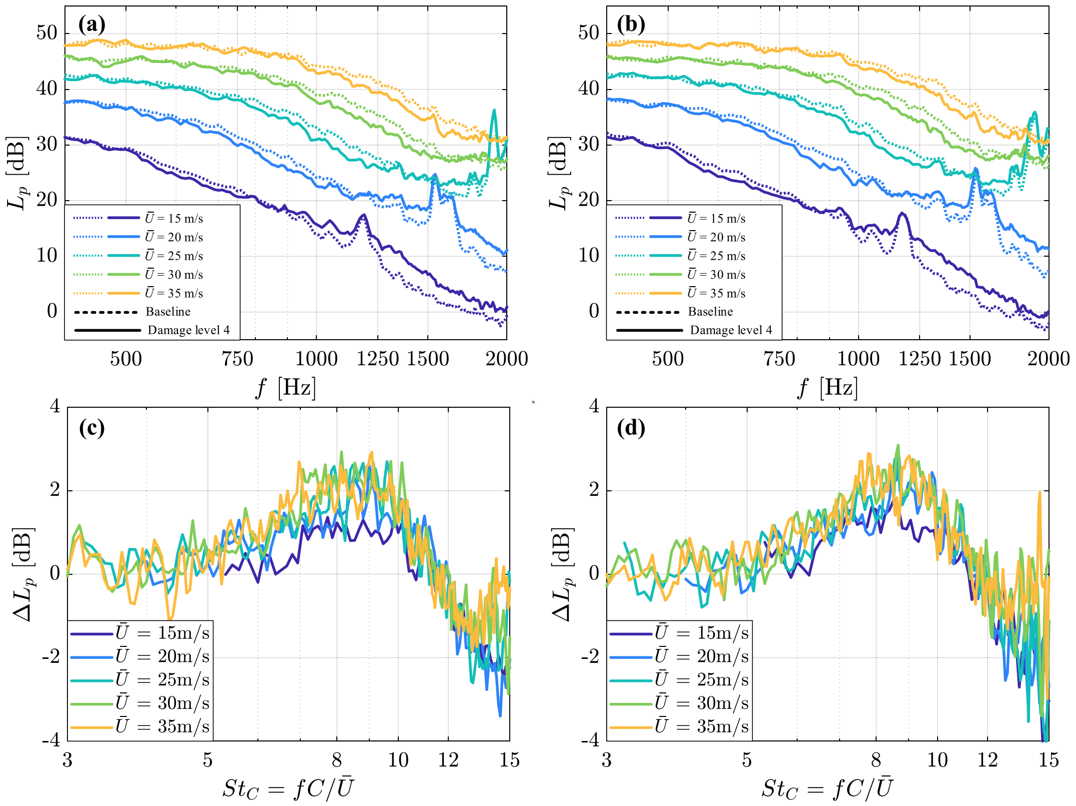

Fig. 19. Sound pressure level of leading edge noise and spectral differences to the baseline for damage level 4 under different mean flow velocity with grid #1 mounted at the angle of attack of 0°: (a) and (c) on the suction side; (b) and (d) on the pressure side.

that the delamination dominates the noise emission. When the airfoil angle of attack is changed, the spectral differences between the damaged case and the baseline are still present from zero lift to stall condition. This indicates that the method is still valid with variable angles of attack. Under turbulent conditions with different mean flow velocities, the reduction in frequency of the impingement noise for the damage case against the baseline is directly proportional to mean flow velocity and the flow velocity does not affect spectral differences between the damage case and baseline.

The experiments were carried out using airfoil models but the conclusions derived from this study are expected to be valid when extend to rotating systems. This relies on the fact that the rotation does not essentially change the mechanisms of the noise generation [77]. However, in real applications, the blades may encounter more complicated situations, for example, the accretion of ice or pollution of the insects or dust on the leading edge. In this case, the noise spectra might be similar to the ones due to the leading edge erosion, which suggests that additional measurements or techniques may be needed for the damage recognition. Further investigations on the small wind turbines in the wind tunnel and in-service wind turbines in wind farms will be carried out in the future. It is worth noting that the experiment was conducted under low Reynolds numbers. In a real application, laminar boundary layer instability noise can be difficult to detect between the middle and tip sections of the blades. Thus, the conclusions derived from the laminar boundary layer instability noise mechanism in this study may only be applied to the blade root section. On the other hand, the turbulence length scales of the turbulent inflow may affect the reduction frequency of the impingement noise. In this study, the turbulence length scales of the turbulent flow when two grids were mounted were of a similar magnitude (~10 mm) thus the effect of the turbulence length scale was not discussed in this study and will be investigated in the future.

CRediT authorship contribution statement

Yanan Zhang: Conceptualization, Methodology, Data curation, Investigation, Formal analysis, Validation, Software, Visualization, Funding acquisition, Writing – original draft. **Francesco Avallone:** Methodology, Investigation, Formal analysis, Resources, Supervision, Writing – review & editing. **Simon Watson:** Methodology, Formal analysis, Supervision, Project administration, Writing – review & editing.

Data availability

Data will be made available on request.

Declaration of Competing Interest

The authors declare the following financial interests/personal relationships which may be considered as potential competing interests: Yanan Zhang reports financial support was provided by China Scholarship Council.

Acknowledgements

This work was supported by the China Scholarship Council (CSC) under Grant 201906330095. The authors would like to thank Dr. Salil Luesutthiviboon, Dr. Riccardo Zamponi, Dr. Daniele Ragni for their suggestions on experimental design and data processing and Dr. Marios Kotsonis, Kaisheng Peng and Stefan Bernardy for their help with the experimental setup.

References

[1] Slot HM, Gelinck ERM, Rentrop C, Van der Heide E. Leading edge erosion of coated wind turbine blades: review of coating life models. Renew Energy 2015;80:837–48. https://doi.org/10.1016/j.renene.2015.02.036.

[2] Bartolomé L, Teuwen J. Prospective challenges in the experimentation of the rain erosion on the leading edge of wind turbine blades. Wind Energy 2019;22:140–51. https://doi.org/10.1002/we.2272.

[3] Law H, Koutsos V. Leading edge erosion of wind turbines: Effect of solid airborne particles and rain on operational wind farms. Wind Energy 2020;23:1955–65. https://doi.org/10.1002/we.2540.

[4] Sareen A, Sapre CA, Selig MS. Effects of leading edge erosion on wind turbine blade performance. Wind Energy 2014;17:1531–42. https://doi.org/10.1002/we.1649.

[5] Han W, Kim J, Kim B. Effects of contamination and erosion at the leading edge of blade tip airfoils on the annual energy production of wind turbines. Renew Energy 2018;115:817–23. https://doi.org/10.1016/j.renene.2017.09.002.

[6] Latoufis K, Riziotis V, Voutsinas S, Hatziargyriou N. Effects of leading edge erosion on the power performance and acoustic noise emissions of locally manufactured small wind turbine blades. J Phys Conf Ser 2019:1222. https://doi.org/10.1088/1742-6596/1222/1/012010.

[7] Papi F, Cappugi L, Perez-Becker S, Bianchini A. Numerical modeling of the effects of leading-edge erosion and trailing-edge damage on wind turbine loads and performance. J Eng Gas Turbines Power 2020;142:1–12. https://doi.org/10.1115/1.4048451.

[8] Gaudern N. A practical study of the aerodynamic impact of wind turbine blade leading edge erosion. J Phys Conf Ser 2014:524. https://doi.org/10.1088/1742-6596/524/1/012031.

[9] Kyle R, Wang F, Forbes B. The effect of a leading edge erosion shield on the aerodynamic performance of a wind turbine blade. Wind Energy 2020;23:953–66. https://doi.org/10.1002/we.2466.

[10] Ehrmann RS, White EB, Maniaci DC, Chow R, Langel CM, van Dam CP. Realistic leading-edge roughness effects on airfoil performance. 31st AIAA Appl Aerodyn Conf 2013:1–19. https://doi.org/10.2514/6.2013-2800.

[11] Watson S, Moro A, Reis V, Baniotopoulos C, Barth S, Bartoli G, et al. Future emerging technologies in the wind power sector: a European perspective. Renew Sustain Energy Rev 2019;113:. https://doi.org/10.1016/j.rser.2019.109270109270.

[12] Eisenberg D, Laustsen S, Stege J. Wind turbine blade coating leading edge rain erosion model: Development and validation. Wind Energy 2018;21:942–51. https://doi.org/10.1002/we.2200.

[13] Al-Hadad M, McKee KK, Howard I. Vibration characteristic responses due to transient mass loading on wind turbine blades. Eng Fail Anal 2019;102:187–202. https://doi.org/10.1016/j.engfailanal.2019.04.006.

[14] Sierra-Pérez J, Torres-Arredondo MA, Güemes A. Damage and nonlinearities detection in wind turbine blades based on strain field pattern recognition. FBGs, OBR and strain gauges comparison. Compos Struct 2016;135:156–66. https://doi.org/10.1016/j.compstruct.2015.08.137.

[15] Tang J, Soua S, Mares C, Gan TH. An experimental study of acoustic emission methodology for in service condition monitoring of wind turbine blades. Renew Energy 2016;99:170–9. https://doi.org/10.1016/j.renene.2016.06.048.

[16] Manohar A, Tippmann J, Lanza di Scalea F. Localization of defects in wind turbine blades and defect depth estimation using infrared thermography. Sensors Smart Struct Technol Civil. Mech Aerosp Syst 2012;2012 (8345):83451O. https://doi.org/10.1117/12.915256.

[17] Talbot J, Wang Q, Brady N, Holden R. Offshore wind turbine blades measurement using Coherent Laser Radar. Meas J Int Meas Confed 2016;79:53–65. https://doi.org/10.1016/j.measurement.2015.10.030.

[18] Traylor C, DiPaola M, Willis DJ, Inalpolat M. A computational investigation of airfoil aeroacoustics for structural health monitoring of wind turbine blades. Wind Energy 2020;23:795–809. https://doi.org/10.1002/we.2459.

[19] Solimine J, Niezrecki C, Inalpolat M. An experimental investigation into passive acoustic damage detection for structural health monitoring of wind turbine blades. Struct Heal Monit 2020;19:1711–25. https://doi.org/10.1177/1475921719895588.

[20] Beale C, Niezrecki C, Inalpolat M. An adaptive wavelet packet denoising algorithm for enhanced active acoustic damage detection from wind turbine blades. Mech Syst Signal Process 2020;142:. https://doi.org/10.1016/j.ymssp.2020.106754106754.

[21] Beale C, Willis DJ, Niezrecki C, Inalpolat M. Passive acoustic damage detection of structural cavities using flow-induced acoustic excitations. Struct Heal Monit 2020;19:751–64. https://doi.org/10.1177/1475921719860389.

[22] Beale C, Inalpolat M, Niezrecki C. Active acoustic damage detection of structural cavities using internal acoustic excitations. Struct Heal Monit 2020;19:48–65. https://doi.org/10.1177/1475921719835761.

[23] Arora V, Wijnant YH, De Boer A. Acoustic-based damage detection method. Appl Acoust 2014;80:23–7. https://doi.org/10.1016/j.apacoust.2014.01.003.

[24] Keegan MH, Nash DH, Stack MM. On erosion issues associated with the leading edge of wind turbine blades. J Phys D Appl Phys 2013:46. https://doi.org/10.1088/0022-3727/46/38/383001.

[25] Fazenda BM, Comboni D. Acoustic condition monitoring of wind turbines: Tip faults. 9th Int Conf Cond Monit Mach Fail Prev Technol 2012, C 2012 MFPT 2012 2012;1:109–23. https://doi.org/10.1121/1.4755203.

[26] Chen B, Yu S, Yu Y, Zhou Y. Acoustical damage detection of wind turbine blade using the improved incremental support vector data description. Renew Energy 2020;156:548–57. https://doi.org/10.1016/j.renene.2020.04.096.

[27] Zhang CQ, Gao ZY, Chen YY, Dai YJ, Wang JW, Zhang LR, et al. Locating and tracking sound sources on a horizontal axis wind turbine using a compact microphone array based on beamforming. Appl Acoust 2019;146:295–309. https://doi.org/10.1016/j.apacoust.2018.10.006.

[28] Tu TH, Lo FC, Liao CC, Chung CF, Chen RC. Using wind turbine noise to inspect blade damage through portable device. INTER-NOISE 2019 MADRID - 48th Int Congr Exhib Noise Control Eng 2019:1–5.

[29] Ye Q, Avallone F, Ragni D, Choudhari M, Casalino D. Effect of surface roughness geometry on boundary-layer transition and far-field noise. AIAA J 2021:1–13. https://doi.org/10.2514/1.j059335.

[30] dos Santos FL, Even NA, Botero L, Venner C, de Santana LD. Influence of Surface Roughness Geometry on Trailing Edge Wall Pressure Fluctuations and Noise 2021:1–15. https://doi.org/10.2514/6.2021-2294.

[31] Oerlemans S, Sijtsma P, Méndez LB. Location and quantification of noise sources on a wind turbine. J Sound Vib 2007;299:869–83. https://doi.org/10.1016/j.jsv.2006.07.032.

[32] Gill H, Lee S. Effect of 2D ice accretion on turbulent boundary layer and trailing-edge noise. Int J Aeroacoustics 2022;21:260–85. https://doi.org/10.1177/1475472X221099497.

[33] Szasz RZ, Ronnfors M, Revstedt J. Influence of ice accretion on the noise generated by an airfoil section. Int J Heat Fluid Flow 2016;62:83–92. https://doi.org/10.1016/j.ijheatfluidflow.2016.06.006.

[34] Tam CKW. Discrete tones of isolated airfoils. J Acoust Soc Am 1974;55:1173–7. https://doi.org/10.1121/1.1914682.

[35] Brooks TF, Pope DS, Marcolini MA. Airfoil self-noise and prediction. vol. 1218. National Aeronautics and Space Administration; 1989.

[36] Kingan MJ, Pearse JR. Laminar boundary layer instability noise produced by an aerofoil. J Sound Vib 2009;322:808–28. https://doi.org/10.1016/j.jsv.2008.11.043.

[37] Kobayashi M, Asai M, Inasawa A. Experimental investigation of sound generation by a protuberance in a laminar boundary layer. Phys Fluids 2014:26. https://doi.org/10.1063/1.4894011.

[38] Ye Q, Avallone F, Ragni D, Choudhari M, Casalino D. Effect of surface roughness on boundary layer transition and far field noise. 25th AIAA/CEAS Aeroacoustics Conf 2019 2019. https://doi.org/10.2514/6.2019-2551.

[39] Saric WS, Carrillo RB, Reibert MS. Leading-edge roughness as a transition control mechanism. 36th AIAA Aerosp Sci Meet Exhib 1998. https://doi.org/10.2514/6.1998-781.

[40] Kerho MF, Bragg MB. Airfoil boundary-layer development and transition with large leading-edge roughness. AIAA J 1997;35:75–84. https://doi.org/10.2514/2.65.

[41] Kim D, Lee GS, Cheong C. Inflow broadband noise from an isolated symmetric airfoil interacting with incident turbulence. J Fluids Struct 2015;55:428–50. https://doi.org/10.1016/j.jfluidstructs.2015.03.015.

[42] Lee G-S, Cheong C. Frequency-domain prediction of broadband inflow noise radiating from a finite-thickness airfoil. J Wind Eng Ind Aerodyn 2021;213:. https://doi.org/10.1016/j.jweia.2021.104618104618.

[43] Buck S, Oerlemans S, Palo S. Experimental characterization of turbulent inflow noise on a full-scale wind turbine. J Sound Vib 2016;385:219–38. https://doi.org/10.1016/j.jsv.2016.09.010.

[44] Faria AM, Saab JY, Rodriguez S, de Mattos PM. A rapid distortion theory-based airfoil turbulent inflow noise prediction method. J Brazilian Soc Mech Sci Eng 2020;42:1–9. https://doi.org/10.1007/s40430-020-02468-2.

[45] Amiet RK. Acoustic radiation from an airfoil in a turbulent stream. J Sound Vib 1975;41:407–20. https://doi.org/10.1016/S0022-460X(75)80105-2.

[46] Paterson R, Amiet R. Acoustic radiation and surface pressure characteristics of an airfoil due to incident turbulence 1976. https://doi.org/10.2514/6.1976-571.

[47] Oerlemans S, Migliore P. Aeroacoustic wind tunnel tests of wind turbine airfoils. Collect Tech Pap - 10th AIAA/CEAS Aeroacoustics Conf 2004;3:2758–75. https://doi.org/10.2514/6.2004-3042.

[48] Zhong S, Zhang X, Peng B, Huang X. An analytical correction to Amiet's solution of airfoil leading-edge noise in non-uniform mean flows. J Fluid Mech 2020;882:A291–A. https://doi.org/10.1017/jfm.2019.839.

[49] Staubs JK. Real Airfoil Effects on Leading Edge Noise 2008:1–328.

[50] Gill J, Zhang X, Joseph P. Symmetric airfoil geometry effects on leading edge noise. J Acoust Soc Am 2013;134:2669–80. https://doi.org/10.1121/1.4818769.

[51] Merino-Martínez R, Rubio Carpio A, Lima Pereira LT, van Herk S, Avallone F, Ragni D, et al. Aeroacoustic design and characterization of the 3D-printed, open-jet, anechoic wind tunnel of Delft University of Technology. Appl Acoust 2020:170. https://doi.org/10.1016/j.apacoust.2020.107504.

[52] Zhang Y, Avallone F, Watson S. Wind turbine blade trailing edge crack detection based on airfoil aerodynamic noise: an experimental study. Appl Acoust 2022;191:. https://doi.org/10.1016/j.apacoust.2022.108668108668.

[53] Timmer WA, Van Rooij RPJOM. Summary of the Delft University wind turbine dedicated airfoils. J Sol Energy Eng Trans ASME 2003;125:488–96. https://doi.org/10.1115/1.1626129.

[54] Moghadassian B, Sharma A. Designing wind turbine rotor blades to enhance energy capture in turbine arrays. Renew Energy 2020;148:651–64. https://doi.org/10.1016/j.renene.2019.10.153.

[55] Joseph LA, Borgoltz A, Devenport W. Infrared thermography for detection of laminar-turbulent transition in low—speed wind tunnel testing. Exp Fluids 2016;57:1–13. https://doi.org/10.1007/s00348-016-2162-4.
[56] Drela M. XFOIL: An analysis and design system for low Reynolds number airfoils. Low Reynolds number Aerodyn.. Springer; 1989. p. 1–12.
[57] Oerlemans S, López BM. Acoustic array measurements on a full scale wind turbine. Collect Tech Pap - 11th AIAA/CEAS Aeroacoustics Conf 2005;3:2067–75. https://doi.org/10.2514/6.2005-2963.
[58] Sijtsma P. Phased Array Beamforming Applied to Wind Tunnel and Fly-Over Tests. SAE Tech Pap 2010;2010-Octob:17–9.
[59] Sijtsma P, Merino-Martinez R, Malgoezar AMN, Snellen M. High-resolution CLEAN-SC: theory and experimental validation. Int J Aeroacoustics 2017;16:274–98. https://doi.org/10.1177/1475472X17713034.
[60] Merino-Martínez R, Sijtsma P, Snellen M, Ahlefeldt T, Antoni J, Bahr CJ, et al. A review of acoustic imaging methods using phased microphone arrays: Part of the "Aircraft Noise Generation and Assessment" Special Issue. vol. 10. Springer Vienna; 2019. https://doi.org/10.1007/s13272-019-00383-4.
[61] Bahr CJ, Horne WC. Advanced background subtraction applied to aeroacoustic wind tunnel testing. 21st AIAA/CEAS Aeroacoustics Conf 2015. https://doi.org/10.2514/6.2015-3272.
[62] Sijtsma P, Snellen M. Inverse integration method for distributed sound sources. BeBeC 2018:9–17.
[63] Oerlemans S. Detection of aeroacoustic sound sources on aircraft and wind turbines 2009:1–173.
[64] Serpieri J, Kotsonis M. Flow visualization of swept wing boundary layer transition. In: 10th Pacific Symp Flow Vis Image Process. p. 15–8.
[65] Serdar M, Lyas K, Hakan H, Turul M. Low reynolds number flows and transition. Low Reynolds Number Aerodyn Transit 2012. https://doi.org/10.5772/31131.
[66] Sudhakar S, Karthikeyan N, Suriyanarayanan P. Experimental studies on the effect of leading-edge tubercles on laminar separation bubble. AIAA J 2019;57:5197–207. https://doi.org/10.2514/1.J058294.
[67] Patterson RW, Vogt PG, Fink MR, Munch GL. Vortex noise of isolated airfoils 1972. https://doi.org/10.2514/6.1972-656.
[68] Arbey H, Bataille J. Noise generated by airfoil profiles placed in a uniform laminar flow. J Fluid Mech 1983;134:33–47.
[69] Desquesnes G, Terracol M, Sagaut P. Numerical investigation of the tone noise mechanism over laminar airfoils. J Fluid Mech 2007;591:155–82. https://doi.org/10.1017/S0022112007007896.
[70] Chong TP, Joseph P. "Ladder" structure in tonal noise generated by laminar flow around an airfoil. J Acoust Soc Am 2012;131:EL461–7. https://doi.org/10.1121/1.4710952.
[71] Pröbsting S, Yarusevych S. Laminar separation bubble development on an airfoil emitting tonal noise. J Fluid Mech 2015;780:167–91. https://doi.org/10.1017/jfm.2015.427.
[72] Pröbsting S, Yarusevych S. Airfoil flow receptivity to simulated tonal noise emissions. Phys Fluids 2021;33. https://doi.org/10.1063/5.0045967.
[73] Abo T, Inasawa A, Asai M. Experimental study on the feedback-loop mechanism generating tonal protuberance noise in boundary layers. Eur J Mech B/Fluids 2021;85:46–57. https://doi.org/10.1016/j.euromechflu.2020.08.004.
[74] Dovgal AV, Kozlov VV, Michalke A. Laminar boundary layer separation: Instability and associated phenomena. Prog Aerosp Sci 1994;30:61–94. https://doi.org/10.1016/0376-0421(94)90003-5.
[75] Lysakn PD, Capone DE, Jonson ML. Prediction of high frequency gust response with airfoil thickness effects. J Fluids Struct 2013;39:258–74. https://doi.org/10.1016/j.jfluidstructs.2013.02.006.
[76] Lighthill MJ. On Sound Generated Aerodynamically. II . Turbulence as a Source of Sound Author (s): M . J . Lighthill Source: Proceedings of the Royal Society of London . Series A , Mathematical and Physical Published by: Royal Society Stable URL : http://www.jstor. Proc R Soc London A 1953;222:1–32.
[77] Ffowcs Williams, Hawkings DL. Sound generation by turbulence and surfaces in arbitfrary motion. Philos Trans R Soc London Ser A, Math Phys Sci 1969;264:321–42.